Received 00th January 20xx,
Accepted 00th January 20xx
DOI: 10.1039/x0xx00000x

Lithiophilic carbon scroll as Li metal host with low tortuosity design and "Dead Li" self-cleaning capability

Ruijie Zhu,[a] Huijun Yang,[b] Laras Fadillah,[a] Zetao Xiong,[a] Damian Kowalski, [d,e] Chunyu Zhu,[c, d] * Sho Kitano,[a,d] Yoshitaka Aoki,[a,d] Hiroki Habazaki. [a,d]

ABSTRACT On the way to achieve practical lithium (Li) metal anode for next-generation batteries, the formation and accumulation of inactive "Dead Li" is an unavoidable issue. The accumulation of "Dead Li" leads to increased internal mass-transfer resistance which seriously deteriorates the performance of Li metal batteries during long-term cycling. In this study, by accommodating Li metal into a copper oxide coated carbon scroll host with a vertically aligned framework which possesses a unique low-tortuosity structure, the cyclic stability of Li anode can be significantly improved. It is demonstrated that the mass-transfer resistance and the concentration polarization near the Li metal surface can be greatly alleviated by using this low-tortuosity anode structure design. "Dead Li" that is formed on the electrode's surface can automatically fall into the inner tunnel of the carbon host, endowing the anode with the capability of "Dead Li" self-cleaning. As a result, our new Li electrode can remain electrochemically active even after 1000 h in a symmetric cell measurement at 1 mA cm^{-2} to 1 mA h for 500 cycles. The as-reported structure design of Li anode in this work is compatible with most of the modification technologies that have been applied to conventional Li foil electrodes, making this new Li anode with a great potential to be applied in subsequent Li anode researches.

1. Introduction

Lithium (Li) metal is widely considered to be the most promising anode material for developing high energy density batteries. In comparison with other anode candidates, Li metal has the lowest negative potential (E° (Li^+/Li) =-3.04 V vs standard hydrogen electrode (SHE)),[1] by which the nominal voltage of batteries can be greatly increased. Moreover, as benefiting from its ultra-high capacity (3860 mA h g^{-1}), the use of Li metal anode will significantly reduce the overall weight of batteries, so as to meet the requirement for high energy density.[2]

To achieve viable Li metal anodes, many roadblocks are still lying in front of us. Firstly, the large change in volume could be virtually infinite, because Li metal itself is a "no-host" electrode, electrodeposition of Li metal will cause a huge geometric deformation of the electrode.[3] Secondly, on the surface of Li metal, heterogeneous unstable solid-electrolyte-interphase (SEI) that generates from the decomposition of electrolyte often fails to protect Li metal from unceasing side reactions.[4,5] The SEI layer cannot withstand the deformation of the electrode, thereby the continuous consumption of electrolyte and Li metal occur along with the Li electrodeposition-dissolution process. Thirdly, the growth of dendritic Li crystal increases the risk of internal short circuit, and the thermal runaway may cause severe accidents.[6] Finally, being broken from the large Li crystals and subsequently wrapped by SEI, some unreacted metallic Li will be separated from electronically conductive substrate, resulting in the formation of inactive Li metal lumps which are also known as "Dead Li".[7, 8] The formation of "Dead Li" reduces the reversibility of batteries, so that excessive Li metal and electrolyte must be added to batteries to achieve expected service life.

Current researches for optimizing Li metal anode are focusing on the following strategies: 1) accommodating Li metal in conductive 3D hosts, in order to adapt the volume change of electrode[9-14]; 2) designing lithiophilic substrates for seeding uniform nucleation of Li metal, in order to eliminate the dendritic crystal growth;[15-18] 3) adjusting the concentration or composition of electrolytes to form "dense Li deposition" or stable SEI, in order to improve the Coulombic Efficiency (CE) during electrochemical cycling;[19-21] 4) constructing artificial SEI with high ionic conductivity and high modulus on the surface of Li metal, in order to improve the interface stability at the metal-electrolyte interface.[22-26] Thanks to these efforts made by many researchers, the CE of current Li metal batteries can readily achieve a value higher than 99%.[27] But what is interesting is that only very few studies about "Dead Li" are involved, and most studies have evaded this issue. It is confirmed that the accumulation of "Dead Li" will severely increase the concentration polarization near the Li metal surface and block the Li^+ flux, which negatively influence the already adopted Li metal protection strategies and inevitably damage the performance of the cell.[28,29] Fang et al. has proved that by depositing Li crystals with granular size and less tortuosity the trend of forming "Dead Li" can be reduced, but inactive Li will generate in nearly all cases of Li metal batteries.[30] Valid strategies for alleviating the influence from "Dead Li" accumulation still worth studying.

In this study, we innovate a lithiophilic carbon scroll (LCS), which consists of vertically aligned carbon fibers that are decorated with lithiophilic copper oxide (CuO_x) nanoparticles (NPs). The LCS is used as host for Li metal to develop Li@LCS composite electrode. The carbon scroll host with vertically aligned carbon fibers provides a channel structure which can accelerate the diffusion of Li^+. Considering that the transporting behaviour of ion in the porous electrode network can be described by electrode tortuosity, which is a parameter for describing that how the geometric structure of the electrode hinders ion diffusion. Hence, we consider the LCS skeleton

[a.] *Graduate School of Chemical Sciences and Engineering, Hokkaido University, Sapporo, Hokkaido 060-8628, Japan*
[b.] *National Institute of Advanced Industrial Science and Technology (AIST), 1-1-1, Umezono, Tsukuba 305-8568 Japan.*
[c.] *School of Electrical and Power Engineering, China University of Mining and Technology, Xuzhou, 221116, China*
[d.] *Division of Applied Chemistry, Faculty of Engineering, Hokkaido University, Sapporo 060-8628, Japan.*
[e.] *Faculty of Chemistry and Biological and Chemical Research Centre, University of Warsaw, Zwirki i Wigury 101, 02-089 Warsaw, Poland*
† * E-mail: zcyls@cumt.edu.cn,
Electronic Supplementary Information (ESI) available: [details of any supplementary information available should be included here]. See DOI: 10.1039/x0xx00000x

with channel structure which has no obstruction on the way of ion-transport can be called a low-tortuosity electrode. On one hand, with the synergetic effect between lithiophilic CuO_x and low-tortuosity structure, Li metal can be deposited and accommodated in the carbon matrix with low over-potential and suppressed dendrite growth. On the other hand, the inactive Li lumps that are

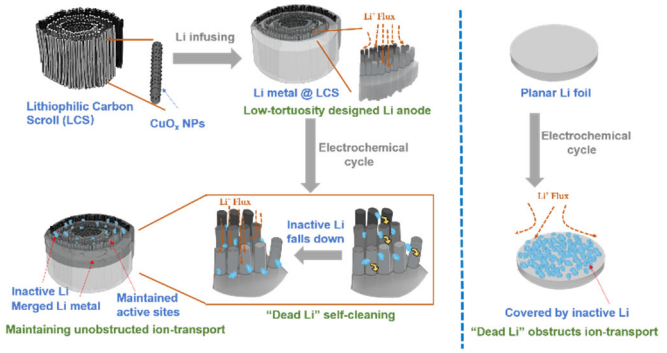

Fig. 1 Schematic illustration for the design concept of vertically aligned lithiophilic carbon scroll host.

formed on the surface of the carbon host will fall into the inner tunnel structure, which plays an important role as a Li reservoir. In this way, the active sites for Li deposition can be always exposed during long-term cycling, as depicted in Fig. 1. As a comparison, conventional Li metal foil with planar structure is easily covered by "Dead Li", which obstructs the ion-transport and severely damages the performance of battery. As a result, the novel low-tortuosity structured Li@LCS electrode can eliminate most of the negative influences from the accumulation of "Dead Li", which is evidenced by the reduced concentration polarization and over-potential. Even after 500 cycles in a symmetric cell measurement at 1 mA cm^{-2} to 1 mA h cm^{-2} for 1000 h, the Li@LCS electrode can still maintain a very low hysteresis voltage of 40 mV vs Li^+/Li. In a Li metal|$LiCoO_2$ full cell, Li@LCS anode ensures the cell capacity hardly be affected by mass transfer resistance as-caused by "Dead Li" accumulation. In contrast, planar Li foil is quickly deactivated due to the influence of "Dead Li" accumulation, by which the cell shows a low-capacity retention.

2. Results and discussion

2.1 Preparation and material properties of the LCS framework and Li anodes

The LCS was prepared through a cotton self-template method. As introduced in Fig. 2, a cotton sheet with one-dimensionally aligned fibers was rolled to a scroll, which had a naturally anisotropic structure with vertically aligned fibers. Subsequently, the cotton scroll was absorbed with the reported "variant of Schweizer's reagent".[31] The above cotton scroll soaked with $[Cu(NH_3)_4]^{2+}$ was pyrolyzed under Ar flow, and the carbon scroll decorated with Cu NPs (CS@Cu) was obtained. The sample was further calcined under air atmosphere at 250 ℃ to make the oxidation of Cu NPs. With the presence of CuO_X species, which were known as the lithiophilic species,[9,33] Li metal could be easily infused into the carbon scroll, forming the Li@LCS composite electrode. In comparison to the conventional isotropic carbon host for Li metal, the anisotropic carbon scroll, which was consisted of vertically aligned carbon fibers, endowed the Li@LCS electrode with a low-tortuosity characteristic, by which the Li^+ transport would be unimpeded.

The structural details of the vertically aligned carbon scroll could be seen in Fig. 3. Fig. 3a-3c present the SEM images of CS@Cu, which has a unique anisotropic structure with vertically arranged carbon fibers, resulting in vertical tunnels of carbon scroll. Due to the decoration of Cu NPs, the colour of CS@Cu is black charcoal mixed with red copper. Thanks to the strong coordination between cellulose and $[Cu(NH_3)_4]^{2+}$, by which the Cu source could be firmly fixed on the fibers surface during heating, the Cu NPs generated from the decomposition of "variant of Schweizer's reagent" are uniform and fine as shown in Fig. 3b. After the oxidation treatment for preparing LCS, the anisotropic structure of carbon scroll was maintained (Fig. 3d), while the colour of LCS was changed to black. EDS spectra confirmed changes in oxygen (O) content of the NPs. A fine Cu NPs decorated carbon substate is shown in Fig. 3e. Mole ratio of O in this region was calculated to be 3.2%, indicating that there is only a small amount of natural oxides layer on the Cu NPs. The Cu NPs were oxidized to larger CuO_x particles after treatment, resulting in the formation of a lithiophilic layer. XRD analysis confirms the composition changes during the preparation, which clearly shows the peaks of Cu (Fig. 3g) that were converted to the peaks of Cu_2O and CuO (Fig. 3h). It is worth pointing out that both CuO and Cu_2O have been confirmed to have lithiophilicity.[9,34] The simultaneous presence of peaks that are corresponded to Cu_2O and CuO in XPS spectra corroborated composition of the LCS (Fig. 3i, 3j). N_2 adsorption behaviour of the samples is shown in Fig. 3k and Fig. S2

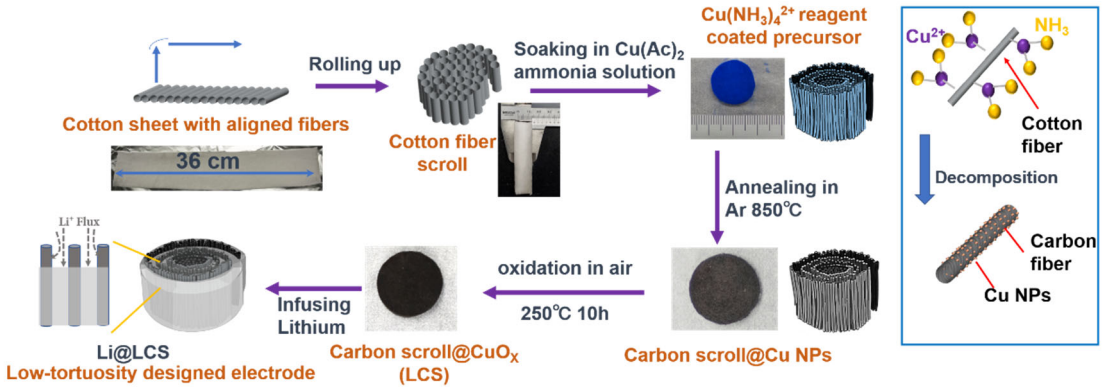

Fig. 2 Schematic diagram for the preparation of low-tortuosity designed vertically carbon matrix and the low-tortuosity designed Li metal anode (Li@LCS).

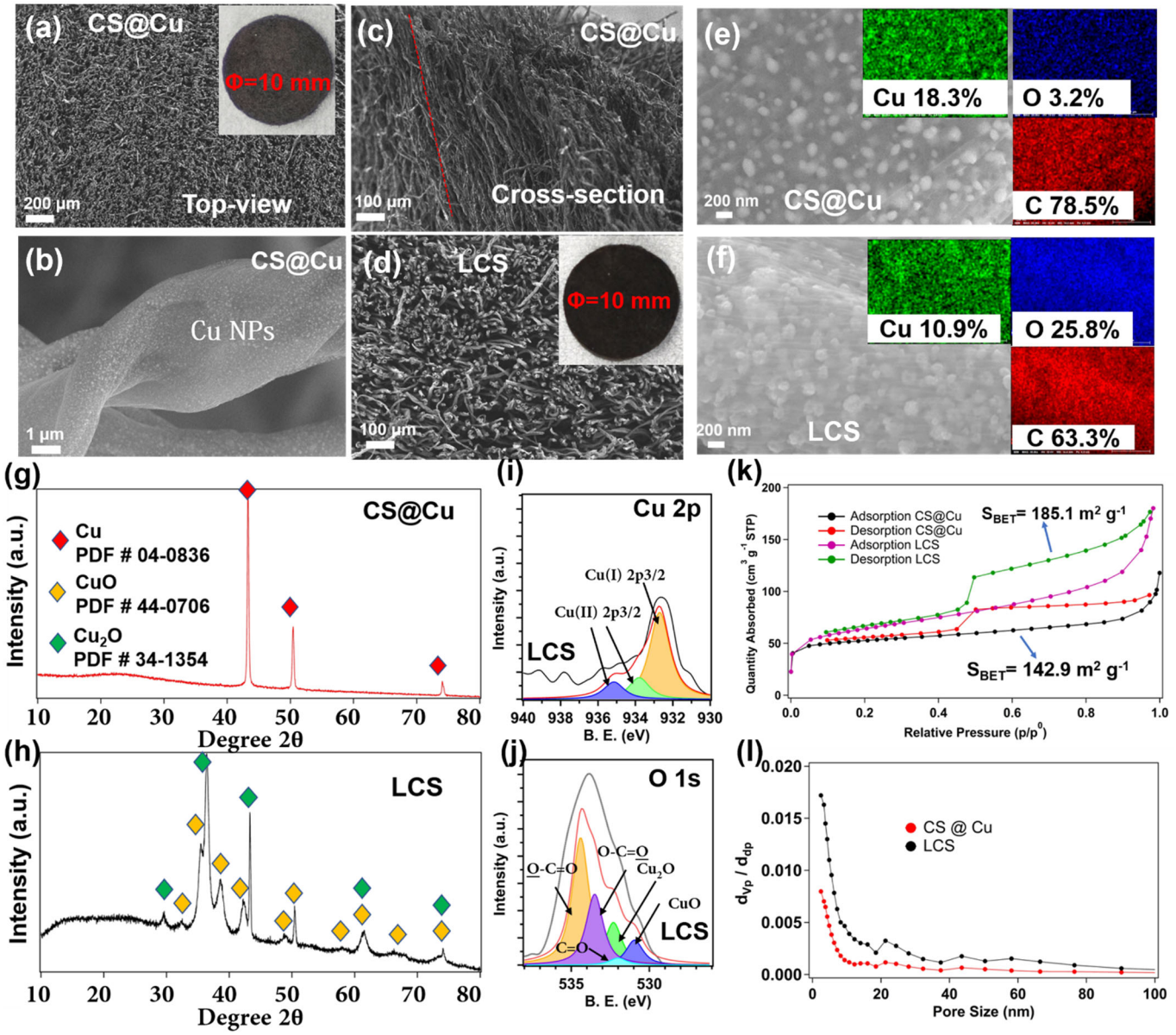

Fig. 3 Material properties of CS@Cu and LCS. SEM images of (a) Top view and (b) a single fiber of the CS@Cu (The inset figure is an optical photo of the CS@Cu disk). Cross sectional SEM observation of (c) CS@Cu. (d) Top view of the LCS (The inset figure is an optical photo of the LCS disk). High magnification SEM and EDS images of (e) a single fiber decorated by fine Cu nanoparticles of CS@Cu and (f) a single fiber decorated by CuO_x nanoparticles of LCS disk. XRD patterns of (g) CS@Cu and (h) LCS. (i) Cu 2p and (j) O 1s XPS spectra for LCS. (k) N_2 adsorption isotherms of CS@Cu and LCS. (l) Pore size distribution of CS@Cu (red) and LCS (black). The material properties for pristine CS are shown in Fig S2 and S3.

Both the CS@Cu and LCS samples exhibit large specific surface area (SSA) of 142.9 $m^2 g^{-1}$ and 185.1 $m^2 g^{-1}$, respectively. In contrast, the pristine carbon scroll without coating presents a very low SSA of 1.6 $m^2 g^{-1}$. The increase in SSA for the Cu decorated carbon scrolls could be attributed to the vigorous pyrolysis of $[Cu(NH_3)_4]^{2+}$ absorbed cotton and the reduction formation of Cu NPs, resulting in the formation of many nanopores. As shown in Fig. S4, Cu NPs were embedded in the nanopores, however, after oxidization treatment, the NPs were squeezed out of the pores due to the volume expansion from Cu to CuO_x and the oxidizing consumption of carbon, resulting in a further SSA increase. The pore-size distribution was calculated by the BJH method as shown in Fig. 3l, indicating the presence of numerous mesopores in the range of around 2 nm to 10 nm**.** At the same time, in order to understand the low-tortuosity characteristics of LCS framework, we compared the difference in tortuosity between LCS and other 3D hosts (Fig. S5-Fig. S8). The relevant results are summarized in Table S1 and Table S2. The tortuosity of conventional carbon cloth is about 6-fold that of LCS, while the tortuosity of horizontally aligned carbon fiber is around 8-fold that of LCS. This shows that LCS can greatly alleviate the hindrance of Li-ion transporting, which makes it a low-tortuosity host.

The lithiophilicity of LCS as-endowed by CuO_x ensures that the carbon scroll host could be directly used to host Li metal. By employing the commonly used melting-infusion method,[35] molten Li could gradually flow into the carbon skeleton and occupy the empty spaces between the fibers (Fig. 4a), thus forming the Li@LCS composite electrode. The surface of the composite electrode

exhibits exposed fibers, as shown in Fig. 4b. This is due to the influence of gravity during the cooling process, in which the liquid Li sank to the bottom of the carbon skeleton. Fig. 4c is a 3D reconstructed image obtained by using a laser scanning confocal microscope (LSCM). It can be seen that the upright carbon fibers maintains a large number of channels on the surface of the electrode, which allows Li-ion can transport smoothly at the electrode surface. A larger magnification SEM image is shown in Fig. S9 to observe the structural details of the electrode surface. The thickness of the Li@LCS composite electrode is around 1300 μm (Fig. 4d). A careful observation of the cross-section of Li@LCS in Fig. 4e indicates that the vertically aligned fibers are wrapped inside Li metal.

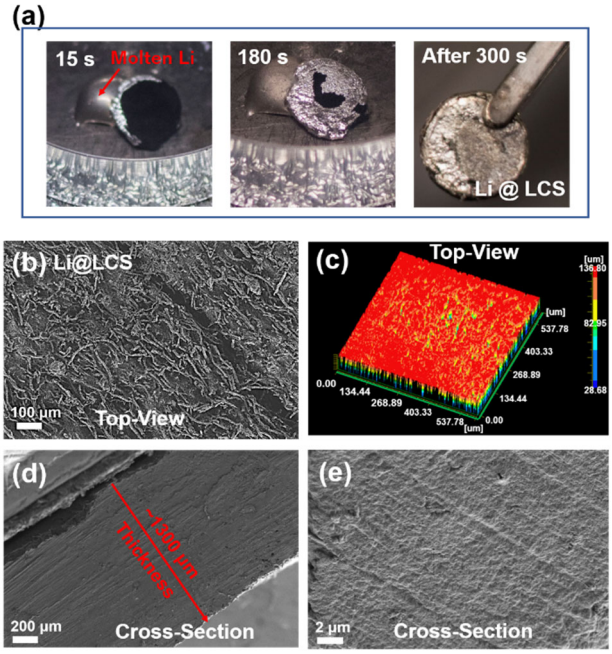

Fig. 4 Morphology and microstructure of the Li@LCS composite electrode. Optical photos (a) for illustrating the melting-infusion process for preparing Li@LCS composite electrode. (b) SEM image and (c) LSCM image of Li@LCS composite electrode from top view. (d, e) SEM images of Li@LCS composite electrode obtained from cross sectional observation.

2.2 Electrochemical properties as measured in symmetric cells and GITT technique

To grasp the uniqueness of the Li@LCS composite electrode in improving the performance of Li anode, the electrochemical cycling performance of symmetric cells was firstly investigated. The electrolyte used in symmetric cell test was 1M LiTFSI in DOL+DME co-solvent, which is a commonly employed electrolyte for Li-S battery. As can be seen in Fig. 5a, the Li@LCS | Li@LCS symmetric cell could maintain a stable cycling performance of at least 500 cycles at a current density of 1 mA cm^{-2} with an areal capacity of 1 mA h cm^{-2}. Here, we stopped the test at the 500th cycle. As shown in Fig. 5b, the Li@LCS symmetric cell could maintain almost the same hysteresis voltage during the 100-400 cycles, with an approximate value of 40 mV. As a comparison, the hysteresis voltage of the Li foil symmetric cell at the 100th cycle was as large as 61 mV. It is also seen that the overpotential of Li foil cell was significantly higher than the Li@LCS cell during the whole cycles. Theoretically, the overpotential of a cell is mainly caused by three parts, namely the ohmic polarization, the activation polarization, and the concentration polarization. Considering that for the symmetric Li metal cells, the activation polarization mainly comes from the following reactions:

$$Li^+ + e^- \longrightarrow Li^0 \quad \text{(Reduction) (1)}$$

$$Li^0 \longrightarrow Li^+ + e^- \quad \text{(Oxidation) (2)}$$

Therefore, when the concentration polarization is eliminated, the overpotential difference of the symmetric cells should be only controlled by the ohmic resistance. It is known that the concentration polarization on the surface of Li metal is mainly from the slowing down of Li^+ diffusion caused by the "Dead Li" accumulation.[29] Based on this point of view, in order to reveal the influence that is from the concentration gradient of Li^+ as-caused by "Dead Li", a galvanostatic intermittent titration technique (GITT) was employed. In this way, the difference in ohmic polarization between different symmetric cells can be revealed. At the same time, the influence from "Dead Li" can also be evaluated. As shown in Fig. 5c, the GITT cycle was obtained after the 500th cycle of Li@LCS symmetric cell corresponding to Fig. 5a. The GITT measurement was conducted by charging (or discharging) at 1 mA cm^{-2} for a short time, which subsequently had a rest for a certain time that was enough for the completion of Li^+ diffusion on the electrode surface. In this manner, the mass-transfer resistance could be eliminated, and the Li^+ concentration near the surface could return to the initial state at each intermittent.[36] This capacity reached a value of 1 mA h cm^{-2}. In this way, we were able to compare the Li-ion concentration polarization of different Li metal electrodes, and to have a deep insight into the role of the LCS skeleton.

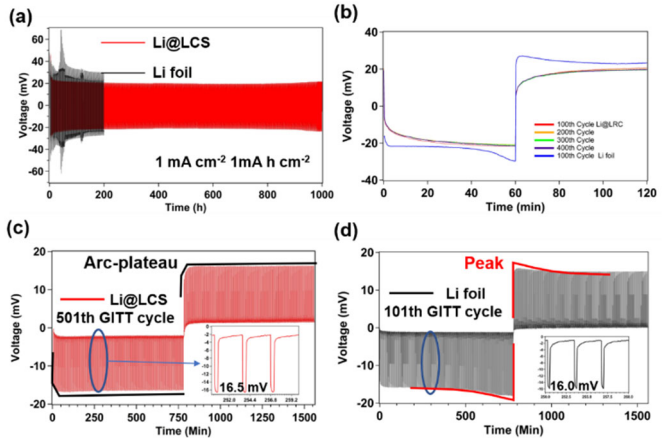

Fig. 5 Electrochemical performance of Li@LCS in ethe r-based LiTFSI electrolyte. (a) Plating/stripping curves in symmetric cell test at a current density of 1 mA cm^{-2} with a capacity of 1 mA h cm^{-2}. (b) Voltage profile of Li@LCS symmetric cell and Li foil symmetric cell at the 100th, 200th, 300th, 400th cycle. GITT measurement of (c) Li@LCS symmetric cell and (d) Li foil symmetric cell (corresponding to Fig. 4a). Here, the GITT measurement was performed after the first 500 cycles (100 cycles for Li foil).

In view of that the Li^+ concentration near the electrode surface is strongly affected by ion mobility and diffusion coefficient. High mass transfer resistance can influence the diffusion coefficient near the electrode surface, leading to a significant Li^+ concentration gradient. In order to understand the changes in the value and trend of the time-dependent overpotential after which the mass transfer resistance was eliminated, a simulation model was employed to describe the relationship between the overpotential and Li-ion concentration distribution on the electrode surface. Hence, we used the Butler-Volmer equation which as modified by Chen et al. as the

electro-deposition model for Li metal.[29] It is reported that when the applied current density is not very high (such as 1 mA cm^{-2}), the modified Butler-Volmer model is more suitable than the conventional Marcus-Hush model.[37] The modified equations are shown as below:

$$j = j_0[\frac{c_{Li^+(surf)}}{c_{Li^+(bulk)}}\exp(-\frac{\beta F}{RT}\eta) - \frac{c_{Li^0(surf)}}{c_{Li^0(bulk)}}\exp(\frac{(1-\beta)F}{RT}\eta)] \quad \text{(Reduction) (3)}$$

$$j = j_0[\frac{c_{Li^0(surf)}}{c_{Li^0(bulk)}}\exp(\frac{(1-\beta)F}{RT}\eta) - \frac{c_{Li^+(surf)}}{c_{Li^+(bulk)}}\exp(-\frac{\beta F}{RT}\eta)] \quad \text{(Oxidation) (4)}$$

Here, j refers to current density and j_0 refers to exchange current density, and β is symmetry factor. $c_{Li+(bulk)}$ and $c_{Li0(bulk)}$ are the bulk concentration of Li^+ and metallic Li, while $c_{Li+(surf)}$ and $c_{Li0(surf)}$ are the surface concentration of Li^+ and metallic Li, respectively. η is overpotential and R, T, F are the ideal gas constant, temperature, Faradays' constant, respectively. Relationship between the applied

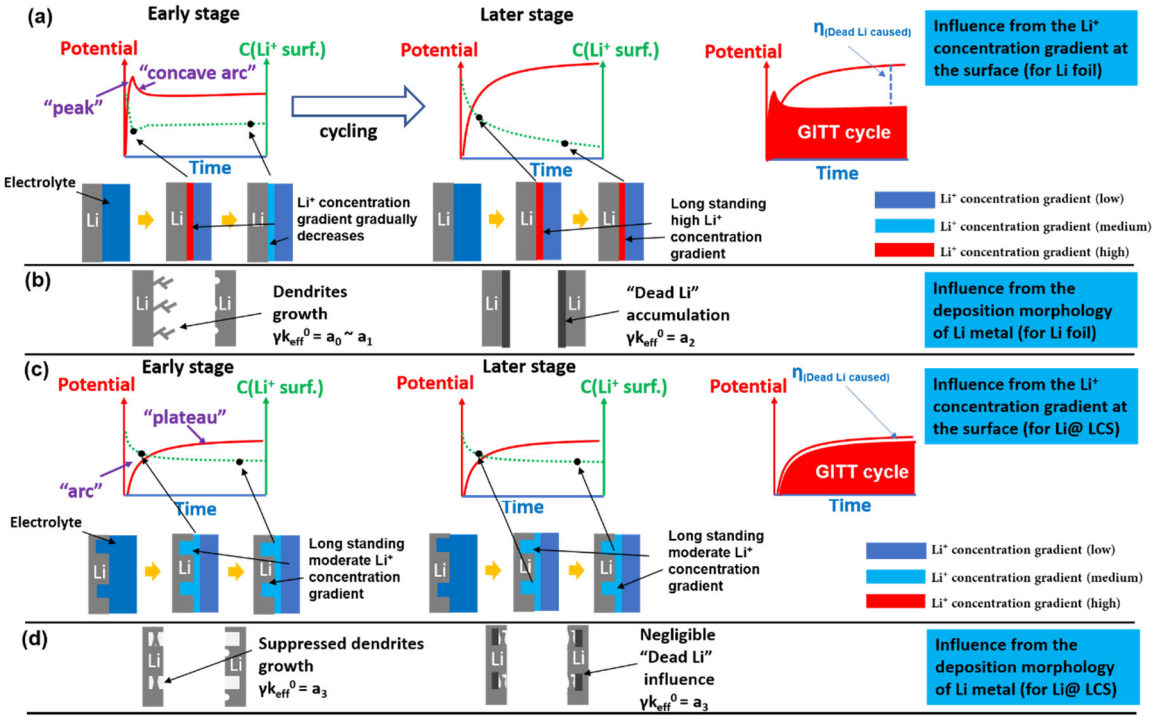

Fig. 6 (a) Schematic illustration for explaining the potential and Li^+ concentration profiles (upper plots) near the electrode surface at initial stage (left), later cycles (mid) and GITT cycle (right), and the corresponding Li-ion concentration distribution near the electrode surface (bottom illustration) in a Li foil symmetric cell. (b) Schematic illustration of the electrode morphologies at initial stage (left) and later cycles (mid), in a Li foil symmetric cell, corresponding to scheme (a). (c) Schematic illustration for explaining the voltage and Li-ion concentration profiles (upper plots) near the electrode surface at initial stage (left), later cycles (mid) and GITT cycle (right), and the corresponding Li-ion concentration distribution near the electrode surface (bottom illustration), in a Li@LCS symmetric cell. (d) Schematic illustration of the electrode morphologies at initial stage (left) and later cycles (mid), in a Li@LCS symmetric cell, corresponding to scheme (c). Potential response of the cell and Li-ion concentration at the reducing side ($Li^+ \rightarrow Li^0$) were plotted vs. time in a half cycle. Deep-blue, cyan-blue and red zones shown in the bottom of schematic (a) and (c) referred to low Li^+ concentration gradient, moderate Li^+ concentration gradient and high Li^+ concentration gradient, respectively.

current, overpotential and Li-species concentration distribution at non-equilibrium conditions is shown intuitively through those equations. Moreover, j_0 can be expressed by the following equation:

$$j_0 = \gamma F k_{eff}^0 \, [c_{Li^+(bulk)}]^{(1-\beta)} \, [c_{Li^0(bulk)}]^{\beta} \quad (5)$$

In which, γ is a parameter representing the roughness of electrode surface, and k_{eff}^0 is an effective heterogeneous rate constant. Both γ and k_{eff}^0 are depending upon the electrode morphology, namely, the morphology of deposited Li metal.

The time-dependent overpotential in a Li metal symmetric cell is influenced mainly by two aspects, i.e., the Li^+ concentration gradient on the surface of electrode and the morphology of the electrode surface. Hence, we summarized the possible situations of Li metal symmetric cells that were tested by us, based on the model given by Chen et al,[29] As shown in Fig. 6(a), when the cell is cycled at an early stage, the electrode surface is not covered by "Dead Li". Once a current is applied to the cell, it will cause a significant concentration polarization on the electrode surface at the initial time, and a high-value initial overpotential will be observed. Then, the Li^+ concentration gradient will gradually recover and become stable, resulting in a relatively low overpotential. Therefore, the time-dependent overpotential of a Li foil | Li foil symmetric cell always shows a "peak" shaped profile at the early stage (Fig. 6(a) left). After

being cycled for a long-time, the electrode surface will be covered by "Dead Li", which will cause a significant Li^+ concentration gradient throughout the cycles, because the diffusion of Li^+ on the electrode surface is hindered. Hence, an arc-shaped potential curve is observed (Fig. 6(a) middle). In the GITT cycle, the influence from "Dead Li" during mass-transferring is eliminated, and the overpotential profile will return to the early-stage status. Here, the overpotential difference is mainly caused by "Dead Li", which is represented as $\eta_{(Dead\ Li\ caused)}$ in the figure (Fig. 6(a) right). The influence from the morphology of electrode surface is shown in Fig. 6(b). When the cell is cycled at the early stage, the growth of Li dendrites will cause a gradually changed γk_{eff}^0, hence the potential profile in this process presents a change of shape from "peak" to "concave arc". But when the cell is cycled at the later stage, the value of γk_{eff}^0 will become relatively stable due to the formation of "Dead Li" layer, thus the shape of the overpotential curve is mainly governed by Li^+ concentration variation.

In the case of Li@LCS electrode, the low-tortuosity structure allows Li^+ concentration gradient near the electrode surface to quickly reach equilibrium after applying current, as depicted in Fig. 6(c). The influence from the morphology of Li electroplating/stripping is depicted in Fig. 6(d). The dendrites-suppressed Li deposition on Li@LCS (shown in Fig. S10, S11 and S13) will result in a stable γk_{eff}^0, therefore the shape of potential curve of Li@LCS symmetric cell should be similar to the "arc-shaped curve" that is shown in Fig. 6(a). However, as benefiting from the low-tortuosity structure, the potential of Li@LCS cell will be lower than Li foil cell. Finally, if the influence of "Dead Li" accumulation is negligible in the case of Li@LCS symmetric cell, the potential curve after long-term cycling and the potential curve of GITT cycle should be consistent with the potential curve of their early stage (Fig. 6(c) right).

The experimental results confirmed our description above. After eliminating the influence from concentration polarization near the electrode surface, the Li@LCS symmetric cell still shows an "arc-plateau" shaped voltage profile, which is similar with the normal voltage profile as shown in Fig. 5b. The overpotential in every "intermittent" is around 16.5 mV, which is close to the over-potential in the initial cycles (~ 20 mV). Although the influence from Li^+ mass-transfer resistance is eliminated in the Li@LCS symmetric cell (during GITT cycle), its overpotential does not show large difference in comparison with the overpotential in normal cycle. This result indicates that the Li@LCS electrode is only affected slightly by the "Dead Li" accumulation during cycling. Furthermore, it is reasonable to consider that the diffusion coefficient of Li^+ near the surface of Li@LCS electrode and the diffusion coefficient in separator (containing electrolyte) are almost the same. At the same time, although overpotential of the Li@LCS cell is not influenced by Li^+ mass-transfer resistance, its "arc-plateau" voltage profile does not change in the GITT cycle, demonstrating that Li deposition on Li@LCS is consistently uniform,[38] because the value of γk_{eff}^0 does not change so much. As a comparison, the GITT cycle for the Li foil symmetric cell was tested after the 100th cycle as shown in Fig. 5d, which indicates an overpotential of 16.0 mV with a "peak" shaped voltage curve. The Li foil symmetric cell has a "Peak" in its voltage profile, and the overpotential drops after the initial concentration gradient achieving an equilibrium, indicating that the time-dependent overpotential in this case is greatly governed by γk_{eff}^0.[29,39] In other words, Li metal crystals that are electrodeposited on Li foil will grow in the form of dendrites. One thing has to be aware of is that the Li^+ diffusion coefficient of ether-based LiTFSI electrolyte is much higher than the diffusion coefficient of carbonate-based $LiPF_6$ electrolyte,[40,41] hence the "Peak" in our work is not as pronounced as those reported in the mentioned literatures.

Electrochemical impedance spectroscopy (EIS) analysis further confirms the abovementioned conclusions. We selected the commonly accepted equivalent circuit to describe the information as-included in EIS. Here, R_{sol} is the electrolyte resistance, R_{SEI} is the resistance of SEI and the R_{CT} is the charge transfer resistance. In Fig. 7a, the Li@LCS symmetric cell shows smaller values of R_{SEI} and R_{ct} than the Li foil symmetric cell before cycling. This is consistent with the conclusion that the Li foil symmetric cell has high overpotential in the initial several cycles. After cycling, R_{SEI} and R_{CT} of both Li@LCS cell and Li foil cell are reduced (Fig. 7b), due to the reason that the SEI generated in the ether-based LiTFSI electrolyte has a relatively good stability and high Li^+ conductivity.[42,43] Moreover, both cells show an overall AC impedance of about tens of ohms, which is consistent with the overpotential value in the symmetric cells test. Detailed observations were provided by directly analyse the electrodes after cycling. As

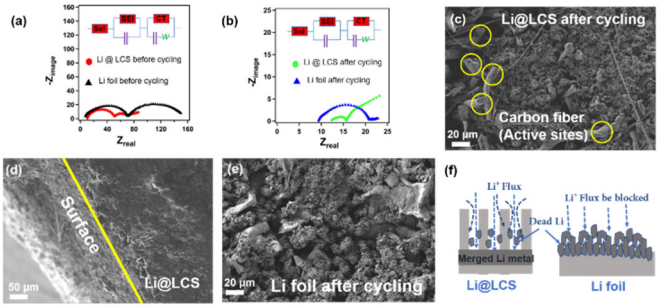

Fig. 7 EIS of Li@LCS symmetric cell and Li foil symmetric cell (a) before and (b) after GITT measurement corresponding to Fig. 5. SEM images of (c, d) Li@LCS composite electrode and (e) Li foil after cycling, corresponding to Fig. 5. (f) Schematic illustration for understanding the accumulation behavior of "Dead Li"on different Li metal electrodes.

shown in Fig. 7c, after 1000 hours cycling, porous Li metal clusters on the surface of the Li@LCS electrode were observed, which were generally considered to be the omen of inactive Li metal generation.[28] This kind of morphology indicates that during long-term Li metal plating/stripping cycling, break of the Li crystal results in incomplete stripping of Li and the generation of "Dead Li". But surprisingly, those porous Li clusters and Li fragments ("Dead Li") did not cover the entire electrode surface. It is observed that most of the vertically aligned fibers are still exposed on the surface of the electrode, and importantly, the tunnels between the fibers are not blocked, indicating that this electrode still has enough active sites for Li deposition and the Li^+ transport path is unhindered. Additionally, the cross-sectional morphology of the cycled Li@LCS electrode is shown in Fig. 7d. A compact and dense Li metal layer that is formed by accumulation of the fallen Li metal blocks can be observed under the yellow line. This observation result is similar with many reported Li metal non-planar 3D hosts,[44,45] indicating that LCS does have the capability to accommodate cycled Li metal into its 3D space, by which the losing of electrochemical activity of Li clusters is avoided.[46] In contrast, the planar Li foil is covered by highly porous "Dead Li" on the surface after cycling, as shown in Fig. 7e. Fig. 7f illustrates the schemes for the formation and accumulation patterns of "Dead Li" during long-term cycling. "Dead Li" is inevitably formed on both Li@LCS and Li foil. In the case of Li@LCS electrode, the deposited Li can be accommodated inside the spaces of the carbon host, at the same time, "Dead Li" will sink into the tunnels under the effect of gravity. Therefore, the LCS host has a unique "Dead Li" self-cleaning capability, and the electrode surface is always active for Li deposition.

In addition, the unique structure of LCS ensures unobstructed Li^+ transport during long-term cycle, and the low-tortuosity structure design of LCS can also eliminate the Li^+ concentration gradient. In contrast, the planar Li foil has to face the hindrance of Li^+ transport as-caused by "Dead Li" accumulation on the electrode's surface. At the same time, the large SSA of the LCS skeleton also dispersed the ion flux and reduced the local current density, which can also efficiently alleviate the dendritic growth of Li metal. The eliminated Li^+ concentration gradient and the lithiophilicity further endow LCS with the capability in suppressing Li dendrite growth.[47] The dendrite-suppressed Li deposition is evidenced by the morphology observation as shown in Fig. S13. Both the dendrite-suppressed morphology and the merging of Li clusters are consistent with previous report given by L. A. Archer's group.[46]

In more symmetric cell tests at harsh conditions, Li@LCS also shows good cycling stability. As shown in Fig. 8a, 8b, when cycled at a current density of 1 mA cm^{-2} with an areal capacity of 2 mA h cm^{-2}, Li@LCS could maintain a superior cyclic stability of more than 400 cycles (> 1600 hours). The overpotential of the Li@LCS symmetric cell is always kept at a low value of around 20 mV from the 100th to 400th cycle. Even when cycled at a higher current density or higher areal capacity as shown in Fig. S14, Li@LCS electrode still presents far better cyclic performance than Li foil. More comparison of the SEM images of the Li anodes after cycling is shown in Fig. S15. In addition, when the orientation of the carbon fiber changed from vertical to horizontal, "Dead Li" accumulation cannot be avoided due to the lack of the space for the "Dead Li" to fall down, as we depicted in Fig. S16.

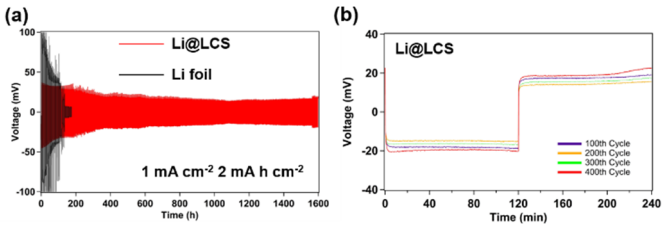

Fig. 8 (a) Symmetric cells tested at a current density of 1 mA cm^{-2} with a capacity of 2 mA h cm^{-2}. (b) Voltage profiles of Li@LCS symmetric cell at 100th, 200th, 300th, 400th cycle.

2.3 Electrochemical performance in full cell measurement

In order to further assess the performance of Li@LCS anode in a full cell, we assembled Li metal|$LiCoO_2$ (LCO) cells by using two kinds of Li anodes, i.e., Li foil and Li@LCS. The electrolyte was $LiPF_6$ in EC/DMC. Compared with electrolytes that are based on ether solvents, electrolytes based on carbonate solvents are less effective in protecting Li metal, especially in the absence of fluorine-containing species (e.g. fluoroethylene carbonate, FEC) as additives .[48] This is to say that the self-protection capability for the Li metal anode will be particularly important to achieve a good cyclic performance in the above full cell measurement. As shown in Fig. 9a, the Li@LCS | LCO cell and the Li foil | LCO cell present close initial capacities of around 148 mA h g^{-1} as-calculated based on the cathode active materials. Here, the corresponding amount of Li metal was excessive both cells. After 300 cycles at a charge/discharge rate of 1 C (150 mA g^{-1}), Li@LCS | LCO cell can maintain a capacity of 102 mA h g^{-1}, while the Li foil | LCO cell shows a low value of only 69 mA h g^{-1}. It is reported that the accumulation of "Dead Li" and the thickening of SEI layer will increase the internal resistance of Li metal | LCO cells.[29,49] The discharging/charging performance of the cathode will be damaged because the discharging/charging voltage platform gradually approach the cut-off voltage during the cycling. This means that once the cell voltage achieves the cut-off voltage, the LCO cathode will not be lithiated/delithiated anymore, even when the LCO is still at an incomplete state of charge. The EIS results as-shown in Fig. 9b confirm that both cells had high internal resistance after 300 cycles. The influence of internal resistance on the cell voltage can be seen intuitively in Fig. 9c, 9d. Since Li_xCoO_2 is considered to be fully lithiated at 3.88 V (vs. Li/Li^+, x=1),[50,51] the difference between discharging platform voltage (V_{dp}) and 3.88 V can be regarded as the overall overpotential (η_o) in the cell. The η_o is consisted of two parts as shown below:

$$\eta_o = 3.88 - V_{dp} = \eta + IR_{sol} \quad (6)$$

Here, η refers to the electrode overpotential, IR_{sol} is the overpotential from electrolyte. Since the IR_{sol} is very small in comparison with η, therefore the IR_{sol} is considered negligible, and the change of η_o approximately reflects the change of electrode overpotential (η). As shown in Fig. 9c, at the 10th cycle, the η_{10th} shows a low value of 0.06 V, demonstrating that the Li@LCS | LCO cell is in good health at the initial several cycles. At the 300th cycle, the η_{300th} is 0.17 V, indicating that the internal resistance of the Li@LCS | LCO cell is increased. In view of the unique "Dead Li" self-cleaning capability possessed by Li@LCS electrode and its low-tortuosity nature, we also adopted the GITT method to eliminate the influence from mass-transfer resistance near the electrode surface, in order to observe the influence from mass-transfer resistance on the overpotential in the Li@LCS | LCO cell. Thus, the η_{GITT} represents the overpotential caused by internal resistance excluding the mass-transfer resistance. The GITT cycle is conducted after the 300th cycle, and the η_{GITT} here shows a value of 0.10 V which is close to the η_{300th}. The difference between 0.17 V and 0.10 V indicates that the mass-transfer resistance caused by "Dead Li" accumulation in the Li@LCS | LCO cell should be around 0.07 V. It is also worth pointing out that the Li | LCO cells are two-electrodes cell rather than three-electrodes cell. Hence, during the GITT cycle, the GITT method also inevitably eliminates the same influence from the cathode side. But according to previous reports,[29] the LCO cathode has a stable performance in $LiPF_6$-carbonate electrolyte. The used testing condition also guaranteed that mainly the influences from the Li metal anode was eliminated during the GITT cycle. Hence, it is reasonable to believe that the result is reliable. As for the voltage profile of the Li foil| LCO cell that is shown in Fig. 9d, the η_{10th} is 0.05 V, indicating that the Li foil| LCO cell also has a good cyclic stability during the first several cycles. Moreover, the η_{300th} is 0.58 V, implying that the cyclic performance of the Li foil| LCO cell gradually deteriorates in subsequent cycles. With the help of GITT, the η_{GITT} of Li foil| LCO cell turns back to 0.15 V, demonstrating that the mass-transfer resistance plays an important role in internal resistance of the Li foil| LCO cell. The obtained values of η are in good agreement with the results form EIS, which strengthens the reliability of our inferences (Fig. 9l). It is also worth pointing out that capacity of the tested cells increases significantly in the GITT cycle. This phenomenon confirms that the internal mass-transfer resistance does cause great damage to the battery capacity, which is also supported by previous study.[29] Voltage profiles of the GITT cycle are shown in Fig. 9e,9f for the Li@LCS | LCO cell and Li foil| LCO cell, respectively. It is clearly to see that the underlying kinetic behaviour revealed by GITT makes the voltage curve turn back to similar shape as the 10th cycle. However, due to the severe ohmic polarization inside the Li foil| LCO cell, which can be caused by the thickening of SEI and cathode electrolyte

interface (CEI), the charging platform voltage of the Li foil cell can hardly achieve 4.2 V. The Li foil cell also exhibits an impaired Coulombic Efficiency owing to the poor Li utilization of Li foil. Cross-sectional SEM observation of the Li metal anodes after cycling further confirmed our speculation. As shown in Fig. 9g, 9h for the Li@LCS electrode, the lithiated carbon fibers remain exposed, and "Dead Li" is not found. As a comparison, the surface of Li foil is covered by "Dead Li" layer with a thickness of around 50 μm (Fig. 9j). The morphology observation results also explain why the η_{GITT} of Li@LCS is smaller than that of Li foil after 300 cycles. As benefiting from the 3D internal space and the dendrite suppressed characteristics, the thickening of SEI is alleviated in the Li@LCS | LCO cell, making the cell exhibits a lower η_{GITT}.

Finally, through the multi-physical simulation of the Li metal | LCO cells, the superiority of Li@LCS composite electrode in alleviating the Li^+ concentration gradient at the electrode surface is intuitively demonstrated. The electrode parameters for simulation were obtained from the 300th cycle corresponding to Fig. 9a. The electrode structure was simplified as presented in Fig. S1. As shown in Fig. 9i, for the Li@LCS | LCO cell, during discharging the Li^+ concentration difference from the electrode surface to the inner part is within 0.1 M. Moreover, the low-tortuosity design similar with the tunnel structure makes the Li^+ concentration gradient at the electrode surface be greatly alleviated.[47,52,53] This result is also confirmed by the corresponding voltage profile shown in Fig. 9c. The simulated discharge voltage profile shows a similar V_{dp} as the actual measured one in 300th cycle, demonstrating the superiority of Li@LCS in alleviating concentration polarization. In comparison, as for the Li foil with a thickness of 50 μm, the "Dead Li" layer shows an extremely strong concentration polarization (Fig. 9k). The simulated voltage curve also indicates a bad performance that is similar with the actual measured curve. This result also illustrates that the blocking of Li^+ transport at the anode side will seriously damage the battery capacity, while the unique low-tortuosity structure design is effective on the cycling stability.

Another full cell measurement in Li-S battery was also conducted with the results shown in Fig. S18, which presents the obvious superiority of the Li@LCS anode.

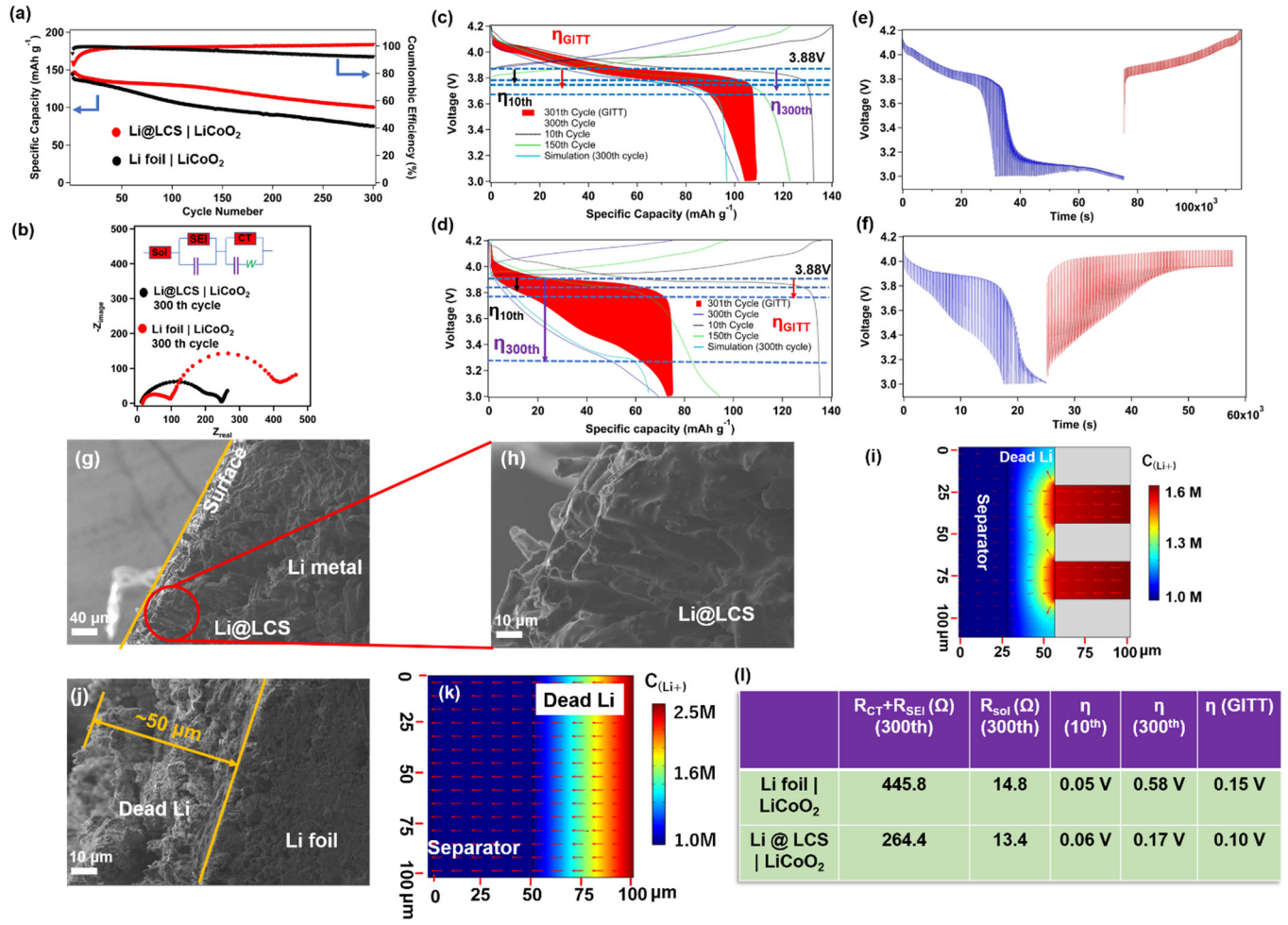

	$R_{CT}+R_{SEI}$ (Ω) (300th)	R_{sol} (Ω) (300th)	η (10th)	η (300th)	η (GITT)
Li foil | $LiCoO_2$	445.8	14.8	0.05 V	0.58 V	0.15 V
Li @ LCS | $LiCoO_2$	264.4	13.4	0.06 V	0.17 V	0.10 V

Fig 9. Electrochemical performance of Li metal | LCO cells in carbonate-based $LiPF_6$ electrolyte. (a) Cycling capacities of Li metal | LCO full cells tested at a discharge rate of 1 C (150 mA g^{-1}). (b) Nyquist plot of different Li metal | $LiCoO_2$ full cells after cycling. (c) Voltage-capacity curves of Li@LCS | $LiCoO_2$ full cell at 10th cycle (black), 150th cycle (green), 300th cycle (blue), the GITT cycle (red) and the simulated 300th cycle (cyan-blue). (d) Voltage-capacity curves of Li foil | $LiCoO_2$ full cell at 10th cycle (black), 150th cycle (green), 300th cycle (blue), the GITT cycle (red) and the simulated 300th cycle (cyan-blue). Voltage profile of GITT tests for (e) Li@LCS | $LiCoO_2$ full cell and (f) Li foil| $LiCoO_2$ full cell. (g, h) Cross-sectional SEM images of Li@LCS anode after cycling. (i) Simulation results

of Li^+ concentration distribution near anode surface in the Li@LCS| $LiCoO_2$ full cells at 300th cycle (discharge). (j) Cross-sectional SEM images of Li foil anode after cycling. (k) Simulation results of Li^+ concentration distribution near anode surface in the Li foil | $LiCoO_2$ full cells at 300th cycle (discharge). (l) Internal resistance values and over-potential (η) values of different cells.

3. Experimental section

3.1 Preparation of "variant of Schweizer's reagent" coated cotton scroll precursor

The "variant of Schweizer's reagent" was prepared by dissolving copper acetate hydrate ($Cu(CH_3COO)_2{\cdot}H_2O$, Labchem-Wako) into ammonia solution as reported in our previous studies.[31,32] The concentration of Cu ion was 0.6 M in this report, and the optimization of the concentration is shown in the Supplementary Information. Cotton sheet with aligned fibers was purchased from Suzuran company (Japan, Nagoya). In a typical preparation, a cotton sheet with a length 36 cm was rolled up to a scroll with a diameter of 1.5 cm. The cotton scroll was cut into disks with a thickness of 3 mm. Subsequently, the cotton scroll disks were soaked into the "variant of Schweizer's reagent" for 12 h. After being taken out from the solution, the disks were washed by tetrahydrofuran (THF) for several times in order to remove the excess solution at the surface and the gap. The difference brought by the material synthesis conditions is shown in Fig. S19 and S20.

3.2 Preparation of LCS and Li@LCS composite electrode

The above "variant of Schweizer's reagent" coated cotton scrolls were annealed in Ar flow at 850 ℃ for 1.5 h to obtain the CS@Cu disks, which were polished to a thickness of around 1.3 mm. Afterwards, the CS@Cu disks were calcined in a muffle furnace at 250 ℃ for 10 h, in this way, the LCS disks were obtained. The comparable pristine CS was also prepared by pyrolyzing and annealing the same cotton scroll at 850 ℃ in a tube furnace for 1.5 h. The LCS disks were transferred into a glove-box filled with Ar gas, in which the oxygen level was kept below 0.1 ppm. Pre-polished Li metal was melted on a hot plate at 350 ℃. The LCS disk was put in contact with the molten Li through the bottom in order to make molten Li infiltrate into the skeleton slowly. After carefully taking out the composite, the Li@LCS electrode was obtained.

3.3 Electrochemical test

Metallic Li foil and Li@LCS electrodes were cut into disks with a diameter of 10 mm. Swagelok cells with a 10 mm inner diameter were employed. Symmetric cells were assembled with two identical electrodes. 1 M lithium bis(trifluoromethanesulfonyl)imide (LiTFSI, Kishida Chemical, 99.90%) in 1,3-dioxolane/1,2-dimethoxyethane (DOL/DME, volume ratio 1:1, purchased from Sigma-Aldrich with purity of 99.8% and 99.5% respectively) was used as the electrolyte, and 1 wt% lithium nitrate ($LiNO_3$, Kanto Chemical) was used as an additive. A glass-fiber separator was used, while the added electrolyte amount was 125 µL per cell. Symmetric cells were tested through a galvanostatic Li plating/stripping method, during which the time-dependent overpotential was recorded.

The galvanostatic intermittent titration technique (GITT) test for symmetric cells was conducted by dividing a whole cycle into 480 s. Here, the symmetric cell was charged for 15 s at a current density of 1 mA cm^{-2}, then rested for 3 min for the completion of Li^+ diffusion on the electrode surface. When the overall areal capacity reached 1 mA h cm^{-2}, i.e., after 240 times of charging for a total time of 3600 s, the cell was switched to the discharge mode, and the abovementioned steps were repeated.

Li metal | LCO full cells were assembled by using $LiCoO_2$ cathode and different Li metal anodes. $LiCoO_2$ slurry was prepared by firstly mixing $LiCoO_2$ powders, poly-vinylidene difluoride (PVDF) and acetylene black (AB) with a weight ratio of 8:1:1 in N-methyl-2-pyrrolidone (NMP). The slurry was pasted to an aluminium (Al) foil. After drying, the active material loaded on Al foil was around 2.5 mg cm^{-2}. A disk of $LiCoO_2$ loaded Al foil with a diameter of 10 mm was used as cathode, Li foil or Li@LCS electrode with a diameter of 10 mm was used as Li metal anode. 1 M lithium hexafluorophosphate ($LiPF_6$) in ethylene carbonate/ dimethyl carbonate (EC/DMC 1:1 in volume ratio, Chameleon Reagent) was used as the electrolyte. A glass-fiber separator was used, while the added electrolyte was 125 µL per cell. Li metal | LCO full cells were discharged from 4.2 V to 3.0 V, and charged from 3.0 V to 4.2 V at a constant current. The current density was dependent upon the cathode capacity.

The GITT test for full cells was conducted by intermittently charging (or discharging) the cell until the cell voltage reached the cut-off voltage. Here, the cells were firstly discharged at a current density of 150 mA g^{-1} (calculated by cathode active material) for 15 s which was defined as one section, then the cells rested for 3 min for the completion of Li^+ diffusion on the Li-metal surface. When the cell voltages achieved the cut-off voltage of 3.0 V, the cells were switched to the charge mode, and the abovementioned steps were repeated. For the charge mode, the cells were stopped until that the cell voltages achieved the cut-off voltage of 4.2 V. Otherwise the cells were stopped until the charge section lasted for 480 times, in order to avoid the case that the cells with upper internal resistance cannot achieve the cut-off voltage. The capacity of GITT cycle was the sum of the capacities of all charge or discharge sections. To further verify the Li^+ concentration distribution near anode surface, a multi-physical simulation of the Li metal | LCO cells was conducted using COMSOL Multiphysics (see details in the Supplementary Information).

The electrochemical impedance spectra (EIS) measurement was carried out on a Princeton apparatus with a frequency range from 100 kHz to 0.01 Hz. A multi-channel battery tester (Hokuto Denko, 8CH) was used to test the electrochemical cyclic stability for different Li metal cells. In addition, Li-S full cells, i.e., Li metal | S, were also assembled to further verify the advantages of Li@LCS electrode, and the detailed experiment and results are shown in the Supplementary Information.

3.4 Materials Characterization

Scanning electron microscope (SEM, ZEISS Sigma 500) was used to investigate the morphological information for different samples. For the ex-situ observation of Li@LCS composite electrodes both before and after electrochemical test, the cells were firstly disassembled in Ar filled glove-box, then the Li@LCS electrodes were separated from the sandwiches and washed by DOL/DME co-solvent for several times. For laser scanning confocal microscope (LSCM) observation, the sample is first placed into a chamber with a quartz window to avoid contact between the sample and the air. The sample was then observed through the optical window. X-ray diffraction (XRD) patterns of the samples were recorded by a Rigaku MiniFlex600 X-

ray diffractometer. N_2 absorption/desorption measurement was used to analyse the porous characteristics of the carbon-based materials by using a Microtrac-BEL (BELSORP-mini) surface area analyser. The Brunauer-Emmett-Teller (BET) method was used to calculate the specific surface areas (SSA) of the samples, while the Barrett-Joyner-Halenda (BJH) method was employed to estimate the pore-size distribution.

4. Conclusions

In summary, we prepared a carbon scroll as a novel Li metal host by the pyrolysis of cotton template. The carbon scroll was consisted of vertically aligned carbon fibers, presenting low-tortuosity structure characteristic. Lithiophilic CuO_X NPs were coated on the carbon fibers, making Li metal easily infiltrate into the carbon host to form Li@LCS composite electrode. Li@LCS electrode showed superior electrochemically cyclic stability to the conventional Li foil electrode, especially in alleviating the accumulation of "Dead Li" and reducing the mass-transfer resistance. It was investigated that the inactive Li blocks could naturally sink into the framework of LCS, resulting in an unimpeded Li^+ transport path even in long-term cycling. Moreover, thanks to the low-tortuosity nature and the "Dead Li" self-cleaning capability of the Li@LCS electrode, the decrease in battery capacity which was caused by the upper mass-transfer resistance in the Li | LCO full cell could be significantly reduced. As a result, the Li@LCS electrode delivered a stable cyclic performance of > 1000 hrs in the symmetric cell test at a current density of 1 mA cm^{-2}, and ensured that the Li metal | LCO full cell could maintain a low overpotential during 300 cycles. This work provided a new solution to the problem of "Dead Li" accumulation during the use of Li metal anodes through a simple structural design strategy. In particular, the structure design of Li@LCS electrode is compatible with most of the optimization strategies that have been applied to conventional Li foil, making this research provide efficient inspiration for developing high-performance Li metal anode.

Conflicts of interest

There are no conflicts to declare.

Acknowledgements

A part of the characterization work was conducted at Hokkaido University, supported by the "Nanotechnology Platform" Program of the Ministry of Education, Culture, Sports, Science and Technology (MEXT), Japan. R. Zhu would like to thank the support by Program for Leading Graduate Schools (Hokkaido University "Ambitious Leader's Program"). C. Zhu also thanks the supports by National Natural Science Foundation of China (No. 52006238), Natural Science Foundation of Jiangsu Province (No. BK20200635), China Postdoctoral Science Foundation (2020M681764), and the Fundamental Research Funds for the Central University (Grant no. 2020ZDPYMS24).

Notes and references

1 B. Dunn, H. Kamath and J. M. Tarascon, *Science* 2011, **334**, 928-935.
2 P. G. Bruce, S. A. Freunberger, L. J. Hardwick and J. M. Tarascon, *Nat. Mater.* 2011, **11**, 19-29.
3 G. Zheng, S. W. Lee, Z. Liang, H. W. Lee, K. Yan, H. Yao, H. Wang, W. Li, S. Chu and Y. Cui, *Nat. Nanotechnol.* 2014, **9**, 618-623.
4 G. Bieker, M. Winter and P. Bieker, *Phys. Chem. Chem. Phys.* 2015, 17, 8670-8679.
5 K. Nishikawa, Y. Fukunaka, T. Sakka, Y. H. Ogata and J. R. Selman, *Journal of The Electrochemical Society* 2007, 154, 6.
6 Ulrich von Sacken, Eric Nodwell, Avtar sundher and J. R. Dahn, *Journal of Power Sources* 1995, 54, 240-245.
7 C. Fang, X. Wang and Y. S. Meng, *Trends in Chemistry* 2019, **1,** 152-158.
8 A. Kushima, K. P. So, C. Su, P. Bai, N. Kuriyama, T. Maebashi, Y. Fujiwara, M. Z. Bazant and J. Li, *Nano Energy* 2017, **32**, 271-279.
9 S. Wu, Z. Zhang, M. Lan, S. Yang, J. Cheng, J. Cai, J. Shen, Y. Zhu, K. Zhang and W. Zhang, *Adv. Mater.* 2018, **30**, 1705830.
10 S. Li, Q. Liu, J. Zhou, T. Pan, L. Gao, W. Zhang, L. Fan and Y. Lu, *Advanced Functional Materials* 2019, **29**, 1808847.
11 Y. Ma, B. Yao, M. Zhang, H. Bai and G. Shi, *Journal of Materials Chemistry A* 2018, **6**, 15603-15609.
12 G. Yang, J. Chen, P. Xiao, P. O. Agboola, I. Shakir and Y. Xu, *Journal of Materials Chemistry A* 2018, **6**, 9899-9905.
13 C. P. Yang, Y. X. Yin, S. F. Zhang, N. W. Li and Y. G. Guo, *Nat. Commun.* 2015, **6**, 8058.
14 J. Gao, X. Cai, J. Wang, M. Hou, L. Lai and L. Zhang, *Chemical Engineering Journal* 2018, **352**, 972-995.
15 H. Duan, J. Zhang, X. Chen, X. D. Zhang, J. Y. Li, L. B. Huang, X. Zhang, J. L. Shi, Y. X. Yin, Q. Zhang, Y. G. Guo, L. Jiang and L. J. Wan, *J. Am. Chem. Soc.* 2018, **140**, 18051-18057.
16 B. Yu, T. Tao, S. Mateti, S. Lu and Y. Chen, *Adv. Funct. Mater.* 2018, **28**, 1803023.
17 R. Zhang, X. R. Chen, X. Chen, X. B. Cheng, X. Q. Zhang, C. Yan and Q. Zhang, *Angew. Chem. Int. Ed.* 2017, **56**, 7764-7768.
18 X. Chen, X. R. Chen, T. Z. Hou, B. Q. Li, X. B. Cheng, R. Zhang and Q. Zhang, *Sci. Adv*. 2019, **5**, 7728.
19 X. Fan, L. Chen, X. Ji, T. Deng, S. Hou, J. Chen, J. Zheng, F. Wang, J. Jiang, K. Xu and C. Wang, *Chem* 2018, **4**, 174-185.
20 Y. Yan, Y. M. Zhang, Y. T. Wu, Z. Z. Wang, A. Mathur, H. C. Yang, P. Chen, S. Nair and N. Liu, *ACS Applied Energy Materials* 2018, **1**, 6345-6351.
21 X. Ren, S. Chen, H. Lee, D. Mei, M. H. Engelhard, S. D. Burton, W. Zhao, J. Zheng, Q. Li, M. S. Ding, M. Schroeder, J. Alvarado, K. Xu, Y. S. Meng, J. Liu, J.-G. Zhang and W. Xu, **Chem** 2018, **4**, 1877-1892.
22 N. W. Li, Y. X. Yin, C. P. Yang and Y. G. Guo, *Adv. Mater.* 2016, **28**, 1853-1858.
23 Y. Liu, D. Lin, P. Y. Yuen, K. Liu, J. Xie, R. H. Dauskardt and Y. Cui, *Adv. Mater.* 2017, **29**, 1605531.
24 H. Duan, Y. X. Yin, Y. Shi, P. F. Wang, X. D. Zhang, C. P. Yang, J. L. Shi, R. Wen, Y. G. Guo and L. J. Wan, *J. Am. Chem. Soc.* 2018, **140**, 82-85.
25 M. S. Kim, J.-H. Ryu, Deepika, Y. R. Lim, I. W. Nah, K.-R. Lee, L. A. Archer and W. Il Cho, *Nat. Energy* 2018, **3**, 889-898.
26 T. Zhang, Y. Wang, T. Song, H. Miyaoka, K. Shinzato, H. Miyaoka, T. Ichikawa, S. Shi, X. Zhang, S. Isobe, N. Hashimoto and Y. Kojima, *Joule* 2018, 2, 1522-1533.
27 J. Wang, Y. Yamada, K. Sodeyama, E. Watanabe, K. Takada, Y. Tateyama and A. Yamada, *Nat. Energy* 2017, 3, 22-29.
28 C. Jin, T. Liu, O. Sheng, M. Li, T. Liu, Y. Yuan, J. Nai, Z. Ju, W. Zhang, Y. Liu, Y. Wang, Z. Lin, J. Lu and X. Tao, *Nature Energy,* 2021, **6**, 378-387.
29 K.-H. Chen, K. N. Wood, E. Kazyak, W. S. LePage, A. L. Davis, A. J. Sanchez and N. P. Dasgupta, *Journal of Materials Chemistry A* 2017, **5**, 11671-11681.
30 C. Fang, J. Li, M. Zhang, Y. Zhang, F. Yang, J. Z. Lee, M. H. Lee, J. Alvarado, M. A. Schroeder, Y. Yang, B. Lu, N. Williams, M.

Ceja, L. Yang, M. Cai, J. Gu, K. Xu, X. Wang and Y. S. Meng, *Nature* 2019, **572**, 511-515.
31 R. Zhu, N. Sheng, Z. Rao, C. Zhu, Y. Aoki and H. Habazaki, *Journal of Materials Chemistry A* 2019, **7**, 27066-27073.
32 R. Zhu, C. Zhu, N. Sheng, Z. Rao, Y. Aoki and H. Habazaki, *Chemical Engineering Journal* 2020, **388**, 124256.
33 Q. Zhang, J. Luan, Y. Tang, X. Ji, S. Wang and H. Wang, *Journal of Materials Chemistry A* 2018, **6**, 18444-18448.
34 Y. Liu, S. Zhang, X. Qin, F. Kang, G. Chen and B. Li, *Nano Lett.* 2019, **19**, 4601-4607.
35 Z. Liang, D. Lin, J. Zhao, Z. Lu, Y. Liu, C. Liu, Y. Lu, H. Wang, K. Yan, X. Tao and Y. Cui, *Proc. Natl. Acad. Sci.* 2016, **113**, 2862-2867.
36 Y. Zhu and C. Wang, *Journal of Physical chemistry C* 2010, **6**, 2830-2841.
37 D. T. Boyle, X. Kong, A. Pei, P. E. Rudnicki, F. Shi, W. Huang, Z. Bao, J. Qin and Y. Cui, *ACS Energy Letters* 2020, **5**, 701-709.
38 C. Niu, H. Pan, W. Xu, J. Xiao, J. G. Zhang, L. Luo, C. Wang, D. Mei, J. Meng, X. Wang, Z. Liu, L. Mai and J. Liu, *Nat. Nanotechnol.* 2019, **14**, 594-601.
39 K. N. Wood, E. Kazyak, A. F. Chadwick, K. H. Chen, J. G. Zhang, K. Thornton and N. P. Dasgupta, *ACS Cent. Sci.* 2016, **2**, 790-801.
40 A. Nyman, M. Behm and G. Lindbergh, *Electrochimica Acta* 2008, **53**, 6356-6365.
41 R. Cao, J. Chen, K. S. Han, W. Xu, D. Mei, P. Bhattacharya, M. H. Engelhard, K. T. Mueller, J. Liu and J.-G. Zhang, *Adv. Funct. Mater.* 2016, **26**, 3059-3066.
42 B. Wu, J. Lochala, T. Taverne and J. Xiao, *Nano Energy* 2019, **40**, 34-41.
43 M. Ue and K. Uosaki, *Current Opinion in Electrochemistry* 2019, **17**, 106-113.
44 Y. Wang, Z. Wang, D. Lei, W. Lv, Q. Zhao, B. Ni, Y. Liu, B. Li, F. Kang and Y. B. He, *ACS Appl. Mater. Interfaces* 2018, **10**, 20244-20249.
45 Q. Yun, Y. B. He, W. Lv, Y. Zhao, B. Li, F. Kang and Q. H. Yang, *Adv. Mater.* 2016, **28**, 6932-6939.
46 J. Zheng, T. Tang, Q. Zhao, X. Liu, Y. Deng and L. A. Archer, ACS Energy Letters 2019, **4**, 1349-1355.
47 H. Chen, A. Pei, J. Wan, D. Lin, R. Vilá, H. Wang, D. Mackanic, H.-G. Steinrück, W. Huang, Y. Li, A. Yang, J. Xie, Y. Wu, H. Wang and Y. Cui, *Joule* 2020, **4**, 938-952.
48 H. Zhang, G. G. Eshetu, X. Judez, C. Li, L. M. Rodriguez-Martinez and M. Armand, *Angew. Chem. Int. Ed.* 2018, **57**, 15002-15027.
49 T. T. Beyene, H. K. Bezabh, M. A. Weret, T. M. Hagos, C.-J. Huang, C.-H. Wang, W.-N. Su, H. Dai and B.-J. Hwang, *Journal of The Electrochemical Society* 2019, **166**, A1501-A1509.
50 G. G. Amatucci, J. M. Tarascon and L. C. Klein, 1996, **143**, 1114-1123.
51 K. Mizushima, P. C. Jones, P. J. Wiseman and J. B. Goodenough, Solid State Ionics 1981, **3/4**, 171-174.
52 C. Chen, Y. Zhang, Y. Li, Y. Kuang, J. Song, W. Luo, Y. Wang, Y. Yao, G. Pastel, J. Xie and L. Hu, *Adv. Energy Mater.* 2017, **7**, 1700595.
53 Y. Zhang, W. Luo, C. Wang, Y. Li, C. Chen, J. Song, J. Dai, E. M. Hitz, S. Xu, C. Yang, Y. Wang and L. Hu, *Proc. Natl. Acad. Sci.* 2017, **114**, 3584-3589.